communications materials

A Nature Portfolio journal

Article

https://doi.org/10.1038/s43246-025-01044-2

Microscopic model of the operation of the single-chalcogenide X-point memory

Paolo Fantini[1] ✉, Andrea Ghetti[1], Enrico Varesi[1], Agostino Pirovano[1], Fabio Pellizzer[1], Dario Baratella[2], Chiara Ribaldone[2], Sebastiano Caravati[2], Davide Campi[2], Marco Bernasconi[2] & Roberto Bez[1]

Ovonic threshold switching is the key process for several applications of chalcogenide alloys including phase change memories and selector elements in cross-points arrays. Very recently, it has been shown that the threshold switching voltage V_T depends on the polarity of the applied field. This feature has been already exploited in the realization of the Single Chalcogenide X-point Memory (SXM) in which a single film of a chalcogenide alloy can serve as both a memory and selector unit. In this work, we provide a microscopic understanding of the polarity-dependent V_T by leveraging electrical and physical measurements, numerical simulations based on technology computer aided design (TCAD) and electronic structure calculations based on density functional theory (DFT). We developed a Graded Band Gap (GBG) model in which an inhomogeneous distribution of localized electronic states in the gap is established by the opposite effect of a strong electric field at the cathode and a high density of electrons in the conduction band at the anode. The model is suitable to reproduce several features of the programming window, including its dependence on temperature, thickness and composition of the chalcogenide alloy. The microscopic understanding that we gained on the SXM operation lays the foundation for important improvements in the memory design and in the selection of better performing alloys for applications in enabling memory technologies.

Chalcogenide amorphous alloys are known to undergo a reversible electronic transition between a high-resistive state (OFF state) and a conductive state (ON state) upon application of a voltage exceeding a threshold value. This process is called Ovonic threshold switching (OTS) after Ovshinsky, who discovered this effect in the late 1960's[1]. Since early 2000s, this feature has been exploited in phase change memory (PCM) devices made of telluride alloys that also undergo a fast and reversible transformation between the amorphous and crystalline phases via Joule heating above the switching event[2–5]. PCMs are being exploited in several enabling technologies such as storage class memories[6,7], embedded memories for microcontrollers[8,9], and devices for neuromorphic and in-memory computing[10–12].

More recently, OTS has attracted widespread interest as a potential technology for selector devices[13,14] in combination with both PCM[15,16] and resistive memories[17]. In the selector device, the chalcogenide alloy undergoes the OTS, but it does not crystallize. More recently, it was found that OTS selectors can also feature a threshold voltage (V_T) that depends on the polarity of the programming pulses[18,19]. It was shown that V_T differs if the reading pulse has the same or opposite polarity with respect to the programming pulse[18–20]. This phenomenon paved the way for the realization of memory devices where just a confined thin film of a chalcogenide glass plays the roles of both the selector and the information storage element. Memory cells exploiting this principle, called selector only memory (SOM), self-selecting memory (SSM), or Single-chalcogenide X-point Memory (SXM), have been presented by leading memory manufacturers[21–23]. A compact 2-terminal SXM device with physical size of less than 20 nm soon appeared as a prototypical SSM element that can be integrated in a 3D multi-tier NAND-like architecture[22]. The characteristics of SXM fit well with the requirements for storage class memories, as they combine the cost structure of a vertical 3D NAND with superior latency, endurance, and bandwidth[22]. A sketch of the operational principle of SXM is shown in Fig. 1.

Despite the rapid technological exploitation of SXM, the physical mechanism behind its operational principle, i.e., the polarity dependent OTS, is not fully understood yet. It was initially proposed that this effect could arise from atomic segregation in the presence of strong electric fields and high currents in the ON-state, with an accumulation of cations at the cathode and of anions at the anode[18,21,24]. The local change in composition would change either the barriers for carrier injection at the electrodes, or the local band gap, or the distribution of defect states within the band gap, which controls the sub-threshold current and then V_T. For instance, it was proposed that the accumulation of Ge at the cathode in $GeSe_x$ selectors might lead to an increase in the population of Ge-Ge bonds, which generates empty states close to the conduction

[1]Micron Technology Inc, Vimercate, Italy. [2]Department of Materials Science, University of Milano-Bicocca, Milan, Italy. ✉e-mail: pfantini@micron.com

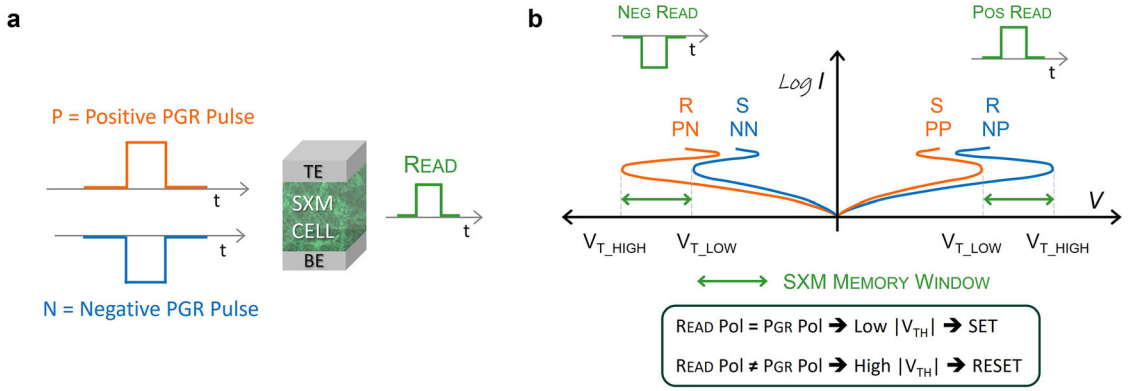

Fig. 1 | Operation of the SXM cell. a Sketch of the positive (P) and negative (N) programming (PGR) pulses with a positive (P) polarity readout pulse. **b** *I*–*V* characteristics and V_Ts illustrating the different programming and readout polarities. V_T is higher when program and read occur in opposite polarity (NP and PN cases), while V_T is lower when program and read have concordant polarity (PP and NN). The different V_T provides the basis for the storage principle of the SXM device.

band[25]. These states, in turn, would increase subthreshold current should electrons injected at the cathode be the main charge carriers. However, evidence of atomic segregation was provided for GeSe at very high operating current[24], while no segregation was found for switching at low current either in GeSe or in multi-component OTS materials like SiGeAsSe that still feature the polarity dependent OTS, as reported in a recent work by Ravsher et al.[26]. The same group recently proposed a new model in which the programming pulse generates in-gap states with an intrinsic anisotropy that respond differently to electric fields of opposite polarity[27]. The nature of these anisotropic structural defects is, however, not clear yet. Moreover, this model is rooted on a particular interpretation of the OTS mechanism itself, which was based on the delocalization/percolation of some localized states in the band gap induced by the electric field at the threshold voltage[28,29]. Another model has been proposed recently for the polarity dependent OTS[30], which is also based on the assumption that OTS is driven by a localized-delocalized transition of some trap in-gap states, although a microscopic identification of these key trap states is not available yet[30]. Most recently, Sung et al.[31] proposed a new model where a non-uniform distribution of hole and electron trap defects is formed and migrates under the strong electric field in the programming process of GeAsSe (GAS) alloys. The hole (electron) traps have been associated with Se-Se (cation-cation) homopolar bonds, by combined deep level transient spectroscopy measurements and electronic structure calculations based on density functional theory (DFT)[31].

In the present work, we propose an alternative microscopic model for the operation of SXM based on experimental electrical measurements supplemented by DFT calculations and by numerical simulations based on Technology Computer Aided Design (TCAD) of GeAsSe alloys offering low leakage current, which is pivotal for large density array, and high thermal stability for 3D stackable cross-point memory integration. The new model, which we name graded band gap (GBG) model, is consistent with the most recent interpretation of the OTS mechanism itself, which is based on a bipolar impact ionization avalanche mechanism[32]. In the presence of a different mobility of electrons and holes, this latter model for OTS is suitable, among other features, to account quantitatively for the observed *S*-type negative differential resistance (NDR)[32]. Once implemented within a TCAD simulation tool, the GBG model can match all the relevant experimental characteristics of the SXM window as a function of the thickness of the active material, of temperature, and of the alloy stoichiometry. A preliminary account of these results was reported in the proceeding of the 2024 International Electronic Device Meeting[33]. The model was developed after providing additional experimental data disproving the role of atomic segregation in the SXM operation, on which we report in the opening of the following section.

Results

Experimental data disproving the segregation model

The SXM operational mechanism was originally interpreted as due to the atomic migration promoting the accumulation of anions (chalcogens, ch) and the depletion of cations close to the anode, and vice versa at the cathode. To mimic this compositional gradient, we fabricated a bi-layered chalcogenide glass device, with ch-rich and ch-poor regions, by using a low thermal budget process to inhibit layer intermixing (Fig. 2a). Ellipsometry measurements on each single layer confirmed the increase of the optical bandgap with chalcogen content (Supplementary Table 1 and Fig. 1). The *I*–*V* characteristics of such stacked capacitors have been measured under both polarities as shown in Fig. 2b.

For the polarity in which the ch-poor layer is at the anode, which should correspond to the readout of the RESET state according to the atomic migration observed in the programmed cells, i.e. opposite polarity with respect to the programming pulse, the *I*–*V* curve shows a higher conductivity than in the other polarity (Fig. 2b). This result is opposite to what expected for the RESET state that must feature lower sub-threshold leakage which is associated with a higher V_T. Figure 2c shows the activation energy for conduction (E_A) as a function of voltage, extracted from the *I*–*V* curves in Fig. 2b at increasing temperatures between 25 °C and 85 °C. The measured E_A is higher for the SET state than for the RESET state. This outcome is consistent with the higher bandgap associated to the ch-rich region and lower band gap associated to the ch-poor region as reported in the inset of Fig. 2c, but, again, it is opposite to what observed in the switched cells that feature a lower E_A for the SET than for the RESET state.

To better assess the element segregation after field-induced switching and its relationship with the polarity dependent switch, we conducted Energy Dispersive X-ray (EDX) measurements on SXM devices[22] with different compositions (Fig. 2d). In general, we observe segregation as reported in several previous works. However, for a particular cell composition, we found a wide SXM window, although no segregation is detected by the EDX scan, as reported in Fig. 2e, f. We remark that in our cells with a lateral size of 20 nm (see "Methods"), the switch involves the whole volume of the cell, and no evidence of filamentary-like conduction is found, as occurs instead in much larger cells. In summary, two independent experimental observations invalidate atomic segregation as the mechanism behind the SXM window proposed in refs. 21,24.

The graded band gap model

We here discuss our new model for SXM, which is based on the presence of a graded band gap (GBG). The formation of this feature in the cell is related to a different response of defect states in the gap to electric fields and to injected currents. The GBG model relies on the recent explanation of the OTS mechanism by a bipolar carrier multiplication model, which is sketched in Fig. 3a[32]. The model is capable of reproducing the *S*-type NDR

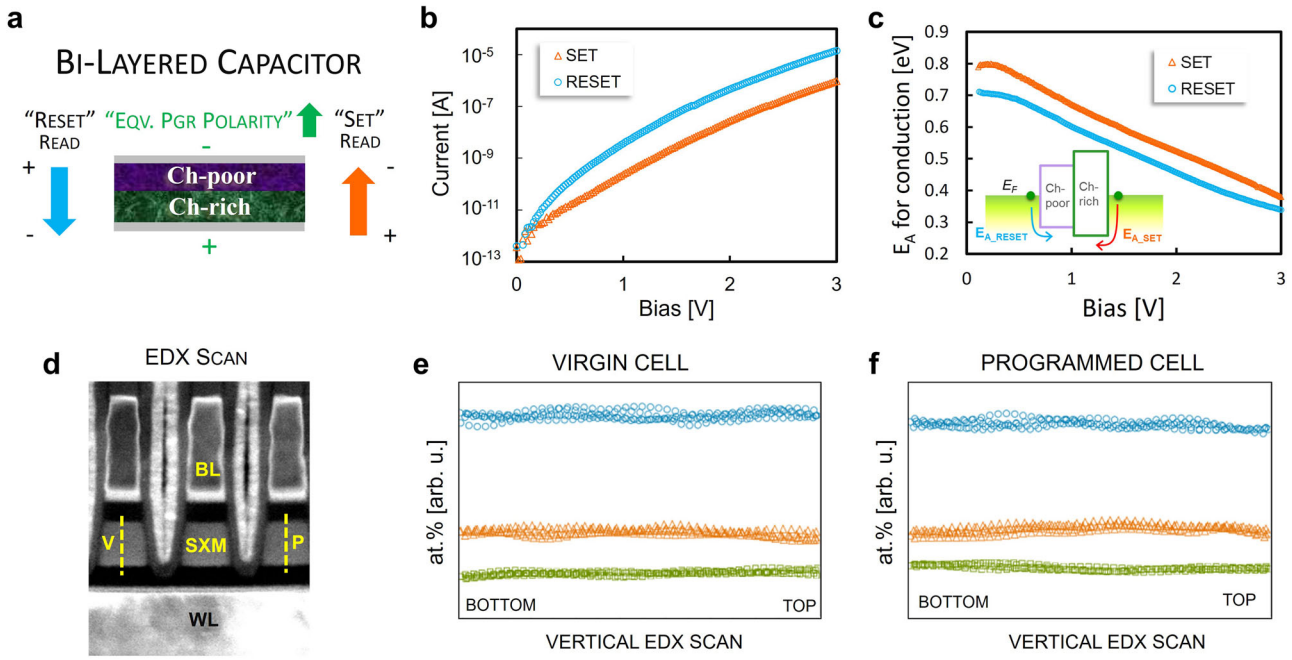

Fig. 2 | Experimental observations invalidating the segregation model. a Bi-layered chalcogenide glass arranged in a capacitor structure to mimic a segregated cell. **b** Polarity dependent *I–V* curves from the bi-layered capacitor shown in (**a**). **c** Activation energy for conduction (E_A) extracted from the polarity dependent *I–V* in **b** measured at different temperatures (see Supplementary Fig. 2). **d** Transmission electron microscopy (TEM) image of a portion of the SXM array fabricated in 20 nm half-pitch technology, including a virgin and a programmed cell. **e** Energy Dispersive X-ray (EDX) scan along the direction of the electric field and current for a virgin cell, as in (**d**). **f** The same of **e** for a polarity programmed cell. No segregation is detected for this specific stoichiometry.

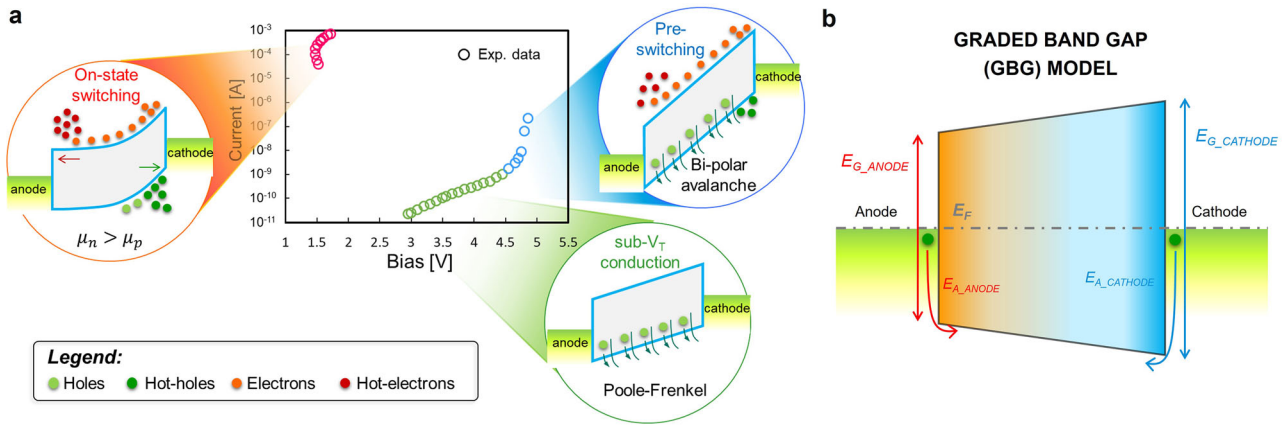

Fig. 3 | Threshold switching model and graded band gap (GBG) model. a Simulated *S*-shaped current-voltage (*I–V*) characteristic by means of the bipolar avalanche model. The schematic band diagrams surrounding the plot describe qualitatively the different conditions: from the low field pre-switching regime up to the bipolar multiplication avalanche that gives rise to the NDR region and the ON-state (adapted from ref. 32). **b** Graded Band Gap (GBG) model responsible for SXM window with the two different activation energies (E_A) for hole injection at the anode and cathode.

current-voltage characteristic by leveraging on three key ingredients, namely (i) the Poole-Frenkel conduction by majority holes at low electric field, (ii) the bipolar avalanche multiplication that triggers the switching regime, and (iii) the large secondary electron mobility compared to the hole mobility leading to the ON-state. The Poole–Frenkel conduction mechanism for holes requires the presence of localized in-gap states close to the mobility edge at the valence band. The band diagram in Fig. 3a of the ON-state switching highlights two anode-cathode asymmetries that occur during the electrical switching of the cell and that are reproduced by our model, i.e., the presence of high density of electrons at the anode and of a high electric field at the cathode. This asymmetry is the pivotal element for our explanation of the SXM operation. In fact, as we will see in the next sections, atomistic simulations show that these different features at the two electrodes have a different impact on the in-gap localized electronic states. Namely, the injection of electrons in localized in-gap states close to the conduction band triggers an irreversible local structural transformation that brings the energy of these localized states closer to the valence band edge. This would lead to an increase in sub-threshold conduction. On the contrary, the presence of a strong electric field causes an irreversible removal of the localized states in the band gap that leads to a decrease in subthreshold conduction. The removal of defect states in the gap by an electric field is also consistent with the acceleration of the drift (increase) in the electrical resistance once the system is stressed by an electric field below threshold. The field-accelerated drift is well documented in literature for the $Ge_2Sb_2Te_5$ phase change alloy[34], and a similar phenomenology is expected to hold for OTS selector alloys as well.

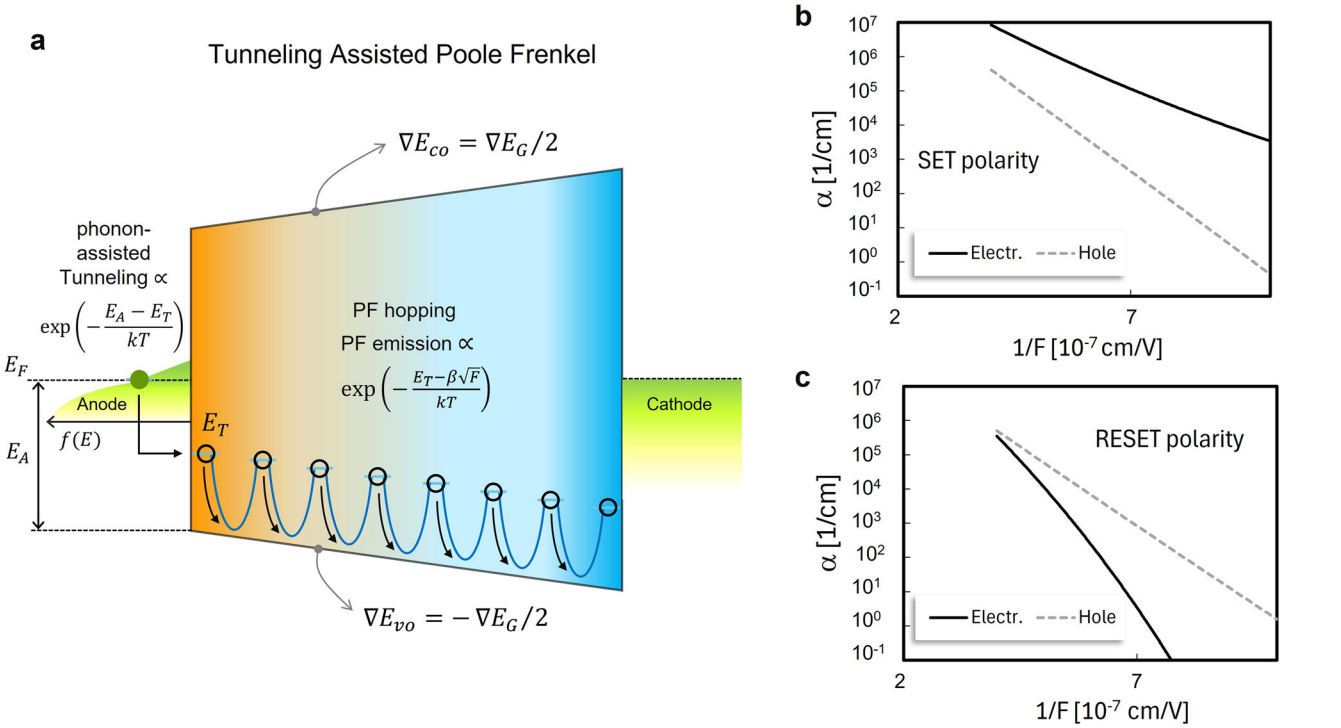

Fig. 4 | Subthreshold conduction mechanism and impact ionization coefficient. **a** Energy-band diagram with a graded band gap giving rise to the gradient of the conduction and valence band edges ~$\nabla E_G/2$. A sketch is given of the Tunneling-Assisted Poole-Frenkel (TAPF) model implemented in our TCAD simulator to describe the sub-threshold current. Estimated impact ionization coefficient α as a function of I/F for electrons and holes for **b** SET and **c** RESET. ∇E_G attenuates the α coefficient for electrons that slows down the bipolar avalanche onset for the RESET, leading to higher V_T.

In our picture, the two combined effects of high density of injected electrons at the anode and high electric field at the cathode give rise to an effective graded band gap with a different activation energy for hole injection at the electrodes. The direction of the band gap gradient is defined by the programming step as sketched in Fig. 3b, and it is responsible for the polarity dependent OTS. In fact, when the read pulse has the same polarity of the programming pulse, holes are still injected at the anode where the activation energy is lower, and then V_T is lower as well. On the contrary, when the read pulse has the opposite polarity, holes are injected at the cathodic side of the programming step, where the activation energy is higher, which leads to a higher V_T. Any switching event refreshes the system by changing the graded band gap according to the programming polarity. This is possible because in the ON-state the system is brought above the glass transition temperature where atomic mobility is sufficiently high to restore a uniform distribution of defects before the combined effects of the high electric field and of electrons injection at the two electrodes freeze the out-of-equilibrium asymmetry created by the switching event, where different structural relaxations and bang gap recovery take place at the two opposite sides of the chalcogenide glass.

In the next section, we will show that the GBG model is able to reproduce the main features of the OTS process in SXM, including the dependence of the SXM window on temperature, composition, and chalcogenide thickness. Atomistic support for the GBG model from DFT simulations will be presented in the subsequent section.

TCAD simulations of the switching process in the graded band gap model

The GBG model has been implemented in a TCAD simulation tool to simulate the SXM operation. The sub-threshold conduction has been described by means of a Tunneling-Assisted Poole-Frenkel (TAPF) mechanism in which carriers with a density of states $f(E)$ are injected into the chalcogenide glass by thermally assisted tunnelling process from the electrodes, while the bulk mobility is controlled by trap-to-trap Poole–Frenkel hopping, involving intermediate transitions into conduction/valence states outside the mobility gap (Fig. 4a)[35]. Such a conduction model also agrees with the polarity dependence of the I–V curves of the bi-layered capacitor reported in Fig. 2. In fact, the activation energy for conduction E_A corresponds to the difference between the Fermi energy and the valence band maximum (lower edge of the mobility gap), which is lower at the ch-poor interface and higher at the high E_G side (ch-rich interface, because of the increase in the band gap with the fraction of chalcogen). Moreover, the bipolar avalanche OTS model has been adapted by considering tilted bands with a band gap gradient (∇E_G). The current I depends on the distance u from the injection electrode as $I = I_o e^{\alpha u}$, where α is the impact ionization (II) coefficient, depending in turn on both ∇E_G (Fig. 4a) and the electric field F, as given by

$$\alpha = A_{e/h} \exp\left(-\frac{E_G(x)}{q\lambda\left(F \pm \nabla E_G \cdot \xi_{e/h}\right)}\right) \quad (1)$$

Here, $A_{e/h}$ is a pre-exponential factor for electrons or holes, q is the electron charge, and λ is the mean free path for II[36]. In particular, the opposite sign of the band gap gradient experienced by electrons with the flipped readout polarity provides the correct SET/RESET V_T dependence (Fig. 4b, c). Overall, our model coherently describes the experimental correlation between leakage current and V_T, i.e., a higher sub-threshold current and lower V_T in the SET than in the RESET state. The model contains just a few parameters, $A_{e/h}$, λ and $\xi_{e/h}$, which have been tuned within a range of physically meaningful values to fit the experimental trends of SXM cells. Figure 5a reports the comparison between the simulated and experimental I–V characteristics for SET and RESET by varying temperature. The change of V_T with temperature in the SET and RESET states is well described by the calibrated temperature dependence of the impact ionization pre-factor $A_{e/h}$ (Eq. 1) in the two states. The model can also reproduce the linear increase of the SXM window with the thickness of the chalcogenide glass as shown in

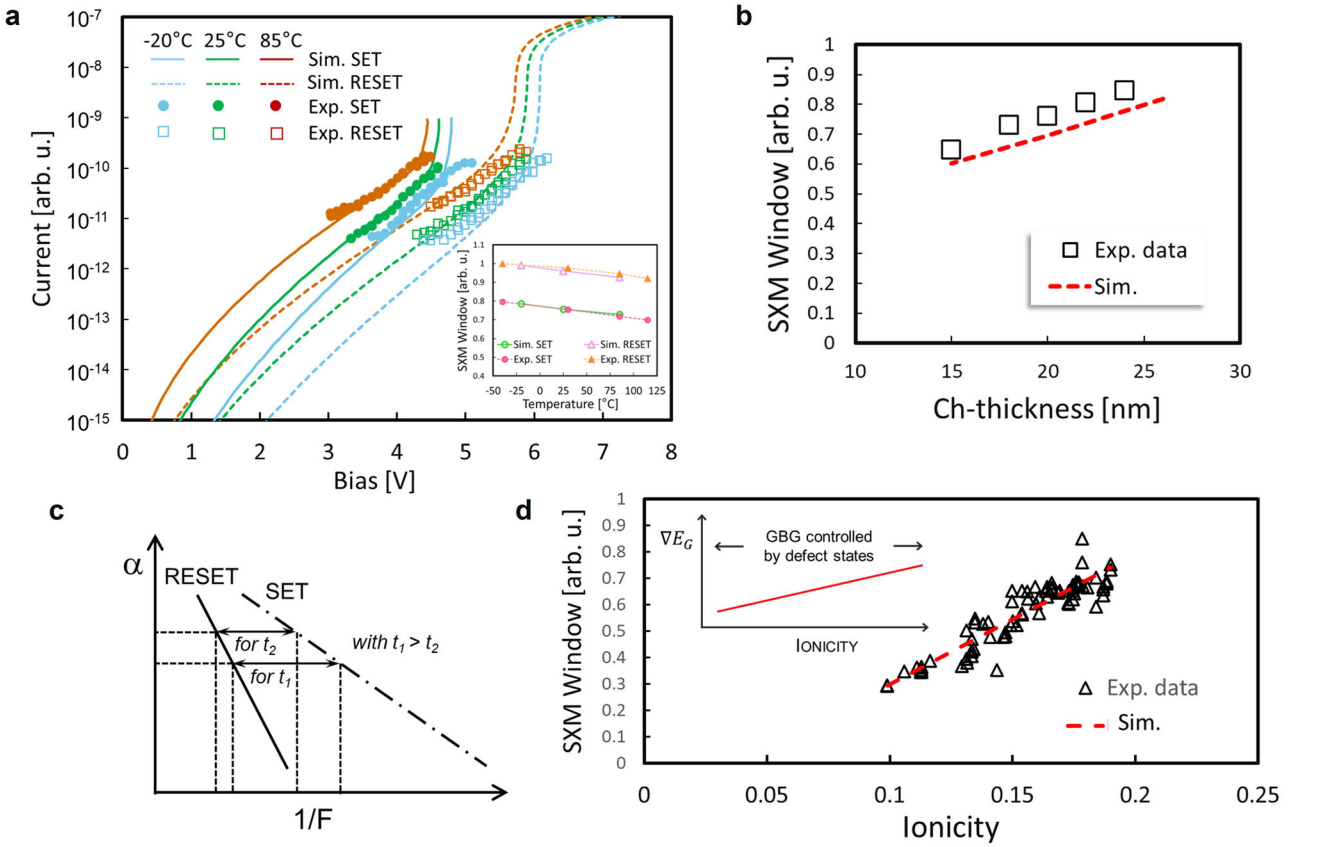

Fig. 5 | TCAD simulations vs experimental trends. a Simulated and experimental *I–V* characteristics for SET and RESET by varying temperature. The simulated and experimental dependence on temperature of V_T for SET and RESET are shown in the inset. **b** SXM window as a function of the thickness of the amorphous chalcogenide film: experimental data and TCAD simulation results are compared. **c** Impact ionization coefficients for SET and RESET as a function of *1/F*; the critical value of α for OTS is shown for two different thicknesses of the chalcogenide film $t_1 > t_2$. **d** Experimental SXM window vs. alloy ionicity calculated as in ref. 36 and TCAD-simulated trend by introducing in the model the linear relation in ∇E_G sketched in the inset.

Fig. 5b. This variation can be understood by considering that the critical value of impact ionization coefficient α dictating the onset of switching increases by decreasing the thickness[32] and that the GBG model yields a different slope of α with the inverse of electric field in the SET and RESET states as shown in Fig. 5c. These two combined effects lead to a lowering of the difference in the threshold electric field for the SET to RESET by decreasing thickness as illustrated in Fig. 5c which ultimately reduces the memory window. Finally, Fig. 5d shows the dependence of polarity window on the alloy ionicity calculated as proposed in ref. 37. In this context, the higher the alloy ionicity, the larger is the effect of the electric field on the removal of the wrong bonds (see next section) responsible of defect states in the gap, which is at the basis of the generation of the SXM window. As we will elaborate further in the next section, defect formation and annihilation modulate the graded band gap that ultimately controls the SXM window. By introducing a linear relation between the gradient of the band gap (∇E_G) and the alloy ionicity, as sketched in the inset of Fig. 5d, TCAD simulations well reproduce the experimental behavior (Fig. 5d).

Atomistic simulations of localized states in the band gap

To support the GBG model described above, we performed DFT molecular dynamics (MD) simulations and analyzed the evolution of the defect states in the gap either under electrons injection or application of a strong electric field. As a prototypical OTS material, we considered the ternary GeAsSe alloy, which is among the most promising materials for selector applications[14,38,39]. In particular, we chose the composition $Ge_{25}As_{30}Se_{45}$ (GAS234), i.e., an off-stoichiometric alloy that lies on the pseudobinary line between Ge and As_2Se_3, namely $Ge_{25}(As_2Se_3)_{15}$. This choice resulted from an extensive DFT analysis of the nature of in-gap states and their dependence on composition in several GeAsSe alloys[40]. As we will see below, in this composition, the in-gap states are mainly localized on Ge-As and As-As bonds. A comparison with other DFT works on the most studied $GeSe_x$ alloys will be discussed later on in this section. Four amorphous models of GAS234 (models M1-M4) were generated in a 300-atom cubic box by quenching from the melt to 300 K within DFT-MD, as described in the Method section. Information on the structural properties of the amorphous models (pair correlation functions, distribution of coordination numbers, partial coordination numbers, percentage of the different types of bonds) is given in Supplementary Figs. 3 and 4 and Supplementary Tables 2 and 3. Se atoms are mostly 2-coordinated with a significant fraction of 3-coordinated atoms; As atoms are 3-coordinated in an overwhelming fraction; Ge atoms are 3- or 4-coordinated with very few atoms 5-coordinated. The geometry of the different local environments is shown in Supplementary Fig. 5, with the type of bonding highlighted by the Wannier functions[41]. Three-coordinated atoms of all species are in a pyramidal geometry, while the large majority of 4-coordinated Ge atoms corresponds to a tetrahedral bonding geometry with sp^3 hybridization (see Supplementary Fig. 5). The 5-coordinated and a minority of 4-coordinated Ge atoms are in a defective octahedral geometry (octahedral bonding angles, but coordination lower than six). The fraction of Ge atoms in a tetrahedral geometry and the fraction of different types of tetrahedra (isolated, corner- and edge-sharing) are given in Supplementary Table 4. As shown in Supplementary Table 3, the majority of bonds are Ge-Se (49.5 %) and As-Se (27 %), but with a non-negligible fraction of As-As (15.5 %) and Ge-As (5.7 %) bonds, while the fraction of Ge-Ge homopolar bonds (2.5 %) is very low. Homopolar bonds and Ge-As bonds are not present in the crystalline form of ternary and binary compounds in the Ge-As-Se phase diagram, and they are therefore often referred to as wrong

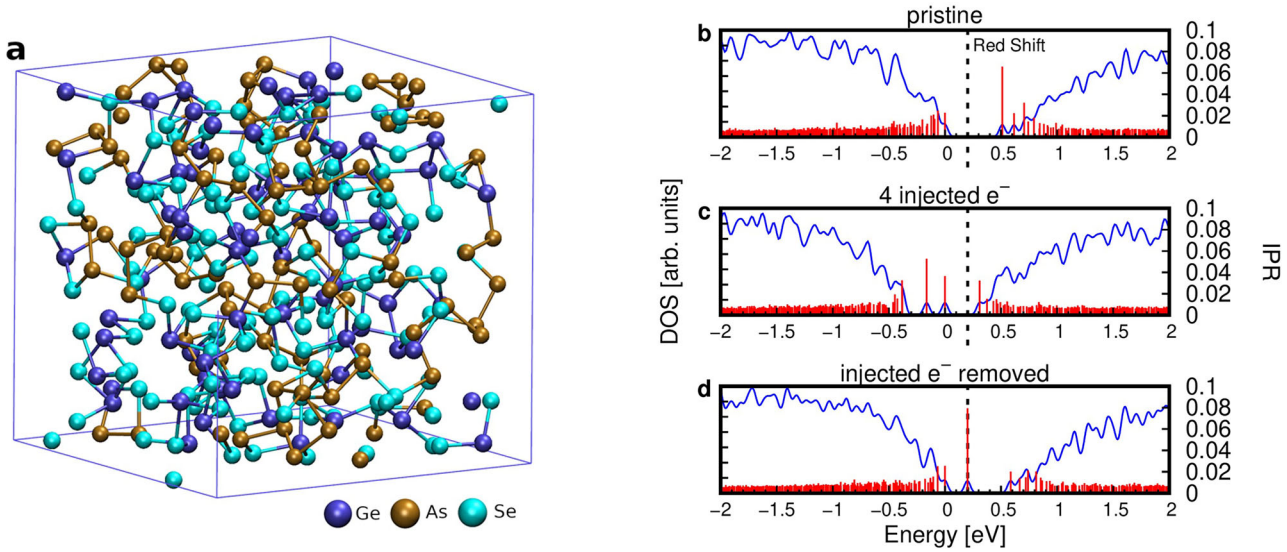

Fig. 6 | Snapshot of the atomistic model of amorphous $Ge_{25}As_{30}Se_{45}$ and its electronic density of states with and without injected electrons. a Snapshot of the atomistic model of a-GAS234. **b** Electronic density of states (DOS) and inverse participation ratio (IPR, red spikes) of model M1 of a-GAS234. The zero of energy is the highest occupied state (top of the valence band or highest occupied molecular orbital, HOMO). The DOS is computed from KS energies at the supercell Γ-point with a 27 meV Gaussian broadening. **c** DOS and IPR with 4 additional electrons, and **d** after removal of the added electrons. The system is relaxed after addition or removal of electrons in (**c**, **d**). The red shift of the in-gap localized state is the signature of the electron-induced irreversible transformation.

bonds. A snapshot of model M1 of amorphous GAS234 (a-GAS234) is shown in Fig. 6a. We remark that both GeSe and $GeSe_2$ exist as stoichiometric crystalline compounds. GeSe crystallizes in an orthorhombic phase (space group Pnma)[42]. The crystal is made of GeSe bilayers in which atoms are 3-fold coordinated in a pyramidal configuration. Interbilayer bonds are mostly due to van der Waals interactions. The formation energy is 60 kJ/mole, and the electronic gap is 1.09 eV[42]. $GeSe_2$ crystallizes instead in a monoclinic phase (space group $P2_1/c$)[43] made of chains of corner- and edge-sharing tetrahedra. The formation energy of 115 kJ/mole and the electronic gap of 2.18 eV[44] for $GeSe_2$ are both larger than in GeSe. For $GeSe_x$ alloys the tetrahedra are thus lower in energy than the pyramidal configurations. The electronic density of states (DOS) for model M1 is superimposed to the inverse participation ratio (IPR) of individual Kohn–Sham (KS) orbitals in Fig. 6b (see "Methods"). The IPR gives a measure of the localization of the KS orbitals as it takes values ranging from 1/N for a completely delocalized electron, where N is the number of atomic-like orbitals in the basis set of the whole supercell, to one for an electron completely localized on a single atomic-like orbital. The state with the highest IPR close to the conduction band edge is localized over a chain of wrong As-As, and As-Ge bonds (As-Se-As-As-As-Ge chain, see inset of Supplementary Fig. 6). Similar features are obtained in the other three independent models of a-GAS234 (models M2-M4) in which the in-gap states with higher IPR are all mostly localized on wrong bonds.

Wrong bonds are weaker than the most abundant Ge-Se and As-Se bonds, forming the bonding matrix, and are thus more sensitive to incomplete relaxation that occurs upon cooling from the melt. As a result, wrong bonds are more prone to give rise to in-gap states. Not all wrong bonds are expected to generate in-gap state, as the localization properties around a bond do not depend only on the nature of the first coordination shell but also on the position and coordination of atoms further apart, as shown for GeSe in ref. 45.

We have then injected additional electrons to our model M1 (compensated by a uniform positive background), aiming at mimicking the condition at the anode during the switching operation, with a high concentration of injected electrons (see section above on the GBG model). The injection of one additional electron in our cell corresponds to an electron density of about $1.2 \times 10^{20}/cm^3$, which it is not too far from the estimate of the density of injected electrons above the threshold in the ON-state of about $6 \times 10^{19}/cm^3$ given by the phenomenological model of ref. 46. We thus optimized the geometry of the amorphous model by adding 2–6 electrons at 0 K. Then, we removed the additional electrons, and we relaxed the system again to see if the transformation induced by the added electrons could survive once the electrons are removed. In Fig. 6, we compare the electronic DOS of the original model (panel b) with the DOS of the system after relaxation with 4 additional electrons (panel **c**) and after removal of the added electrons and further relaxation (panel d). The two empty states close to the conduction band at about 0.5–0.6 eV in Fig. 6b shift close to the valence band and below the zero of energy (highest occupied molecular orbital, HOMO) once four electrons are added, and the system is relaxed (Fig. 6c). The energy of these KS states shifts even closer to the valence band when the electrons are removed at clamped ions, because the energy of an individual KS state depends on its occupation, shifting towards higher energy the larger is the number of electrons that occupy the state at clamped ions. Once the four electrons are removed and the system relaxed (Fig. 6d), the initial DOS is not recovered, which means that the additional electrons have induced irreversible structural transformations that survive once the added electrons are removed. Notice that the lowest unoccupied molecular orbital state (LUMO, i.e., the first empty state) shifts from the edge of the conduction band in the original system to a position close to the valence band after addition and then removal of four electrons. This state keeps its character during the transformation, i.e., a localization on a chain of wrong As-As and As-Ge bonds, as already mentioned above. The transformation leads to local structural relaxations with an energy gain with respect to the original model. Similar results are obtained by adding 2 or 6 electrons. A similar behavior is observed by charging a second independent model of a-GAS234 (model M2). In the third model, instead (model M3), the transformation induced by up to six additional electrons is similar but mostly reversible; the DOS of the original model is, in fact, recovered after removal of the added electrons and relaxation. We must, however, consider that we used a protocol of geometry relaxation at zero temperature that can just find local minima with no activation barrier to overcome. The real system at finite temperature is expected to undergo a transformation lasting up to a few ns in the presence of an electronic current. This time scale is sufficiently long for the system to overcome activation barriers larger than the thermal energy with a sizeable probability. Moreover, we remark that both the initial configuration after quenching and the final configuration after injection and removal of additional electrons are off-equilibrium states. In an ideal glass generated by a quenching/annealing sufficiently slow, we do

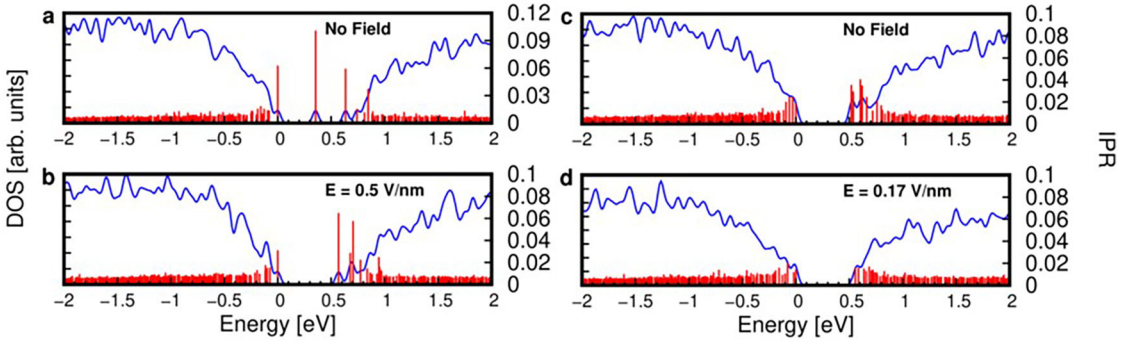

Fig. 7 | Effect of the electric field on the electronic density of states of a-GAS234. Electron density of states (DOS) and Inverse Participation Ratio (IPR, red spikes) of **a** model M4 of a-GAS234 before and **b** after the application and then removal of a 0.5 V/nm electric field. The system was relaxed in the presence of the electric field and relaxed further after the electric field was removed. **c** DOS and IPR for a single snapshot of a model at 300 K generated by slowly quenching from 500 K to 300 K in the lack or **d** in the presence of an electric field of 0.17 V/nm. The DOS are then computed without the electric field for all configurations.

not expect to see localized states in the gap at all. Finally, we mention that in the fourth model (M4), the shift to lower energy of the LUMO state is reversible when it is filled by two electrons. However, when the system was relaxed after addition and removal of six electrons, this LUMO state disappeared from the gap. This state was initially localized of an under-coordinated (two-fold) As atom within a chain of wrong bonds. The initial DOS was then mostly recovered but for the disappearance of this state due to an irreversible structural transformation occurring only at high electron charging (see "Methods" for further details on this model).

In summary, we have seen examples in which the addition of electrons in localized states in the gap, either deep or close to the conduction band, leads to structural relaxations that survive upon removal of the additional electrons and that bring these empty states closer in energy to the valence band. Therefore, this outcome shows that the electron accumulation at the anode (see Fig. 3a), leading to the occupation of initially empty states, can result in an increase of the subthreshold current due to the shift of empty localized states closer to the valence band. This feature supports the first assumption of GBG model on the behavior at the anode.

We now briefly comment on previous works in literature on the in-gap states in amorphous models of $GeSe_x$ alloys generated by quenching from the melt in DFT-MD simulations. We remark that the nature of the in-gap states is expected to depend on composition (see ref. 14 for a review). Valence-alternation pairs or other Se-related states have been reported in Se-rich $GeSe_{1+x}$ alloys[14], while in $Ge_{50}Se_{50}$ and Ge-rich $Ge_{1+x}Se$ alloys, the empty in-gap states, either deep or at the conduction band edge, are related to Ge-Ge homopolar bonds[28]. The presence of a single Ge-Ge bond or a chain of Ge-Ge bonds is obviously not sufficient to give rise to a localized state. These structural features should, in fact, appear in combination with suitable medium range order (MRO) and under-/over-coordination as shown by the analysis of several models in refs. 45,47. Since Ge-Ge bonds are weaker than Ge-Se bonds, we can conceive that homopolar bonds are more prone to accumulate local stress due to MRO and therefore to assume less favorable bond length, angle, or local environment, giving rise to localized states in the gap. The formation of a polaron-like state in empty localized states after charging with an additional electron was reported in ref. 48 for GeSe. In ref. 48, the charging of electron traps was instead induced by a very high density of electron-hole pairs, involving also the band edges, that leads to a closing of the band gap itself. This sort of metallization process was associated to the increase of the fraction of axial bonds (with bond angles of about 180°), and it was proposed as the mechanism of OTS process itself[49]. Similar behavior was reported for GeSbSe alloys in which the increase in the fraction of axial bonds upon electronic excitation was mostly related to Sb[49]. Similar reduction in the band gap was observed in ref. 50 by adding additional electrons in a model of amorphous Ge_2Se_3. Our results on the redshift in energy of the localized in-gap states once they are charged by electrons due to irreversible structural transformation are overall consistent with the previous accounts in literature on the other selenide alloys summarized above. We remark that our work must be seen as an initial DFT investigation of the electronic properties of GAS, aimed also at producing a database for the development of machine learning potentials for these alloys that would allow generating a large number of small (e.g., 300 atoms) amorphous models at a modest computational cost, to improve the statistics on the in-gap states. This approach has recently been adopted to study in-gap states in some telluride alloys[51].

We have then considered the effect of an external uniform electric field on localized states in the gap. A uniform electric field is introduced within Berry's phase approach by keeping periodic boundary conditions (see "Methods")[52,53] in models M1-M4. We first relaxed the system in the presence of an electric field of increasing strength (0.1, 0.25, and 0.5 V/nm). Then, we removed the field, and we relaxed again the system to investigate eventual irreversible transformations induced by the electric field. We observed a different behavior in the four models. In model M4, the largest electric field (0.5 V/nm) was able to remove irreversibly an in-gap state (LUMO) localized on an under-coordinated (two-fold) As atom within a chain of wrong bonds (see above). The electronic DOS and IPR of model M4 before and after application of the electric field (and relaxation as described above) are compared in Fig. 7a, b. Similarly, a 0.5 V/nm electric field was suitable to remove irreversibly some in-gap states in model M3 (see Supplementary Fig. 7a). In model M1 we observed a non-monotonic behavior of the in-gap states with an overall change which is rather marginal at the highest field (see Supplementary Fig. 7b). In model M2, the behavior is more complex with some states moving up and other moving down in energy (see Supplementary Fig. 7c). Overall, we do observe in two models out of four a removal of in-gap states induced by the electric field. A lower density of in-gap states implies a lower subthreshold current, which is consistent with the second assumption of the GBG model on the behavior at the cathode.

Note that this analysis is based on geometry optimization in the presence of the electric field but at zero temperature. Thus, the structural relaxations leading to the irreversible shift of the in-gap states can take place only if the field removes the energy barrier for the process to occur. The same barrier might be overcome at lower field at finite temperature. To assess this effect, we perform additional simulations in which we switched on the electric field during the quenching from the supercooled liquid phase. The simulations in the presence of an electric field within the Berry's phase approach (see "Methods") can be accomplished only in the presence of a sufficiently large band gap between delocalized states. In the lack of a band gap sufficiently large to prevent a Zener breakdown[54], self-consistency in the solution of KS equation cannot be achieved. Since the supercooled liquid is metallic while the amorphous phase is semiconducting, a metal-semiconductor transition occurs upon cooling. We checked that simulations with a lower electric field of 0.17 V/nm can be performed smoothly up to 500 K. Therefore, from the equilibrated system at 500 K, we started two different simulations at constant temperature, about 35 ps long, the first with no electric field and a second with an electric field of 0.17 V/nm. Then,

we quenched abruptly to 300 K different amorphous models equilibrated at 500 K with or without the electric field. We generated four independent models (Q1–Q4) obtained by quenching from snapshots of the trajectory at 500 K sufficiently separated in time, i.e., at 5, 13, 23, and 35 ps. The models were then equilibrated for about 15 ps at 300 K and finally optimized at zero temperature. The quenching to 300 K was performed for all models without the electric field to mimic a final relaxation at zero bias after the system was stressed by the electric field. The DOS were consequently computed without the electric field for all models, as shown in Supplementary Fig. 8. Overall, one can notice that the electric field has caused a reduction in the number of empty localized states in the gap. Only in model Q1 one finds the enhancement of the localization of a filled state close to the valence band. On the contrary, two empty localized states at about 0.5 eV above the HOMO in model Q1 and one empty localized state at about 0.4 eV in model Q2 disappear in the presence of the electric field. All these states are localized on Ge-Ge and Se-Se bonds. The single KS state at about 0.4–0.5 eV in model Q3 changes character from being localized on a chain of Ge-As-As bonds without the field to a state mostly localized on an As-Se bond with the field. The localized states close to the conduction bands in model Q4 also disappear in the presence of the electric field, and they are instead mostly localized on Ge-As bonds.

Despite the limited statistics, we can attempt to rationalize these outcomes as follows. In an ideal glass, we expect to have a prevalence of the stronger As-Se and Ge-Se bonds. These bonds are highly polar due to the difference in electronegativity of the atoms involved (Pauling electronegativities are 1.8, 2.0, and 2.4 for Ge, As, and Se atoms). Homopolar Ge-Ge, As-As, and Se-Se bonds and less polar Ge-As bonds are weaker, and structural transformations, also responsible for aging, are supposed to remove these wrong bonds, leading to the formation of the more polar As-Se and Ge-Se bonds. We can thus speculate that the effect of the electric field is a further stabilization of the polar bonds, which allows for a reduction of the activation barriers to be overcome for the removal of wrong bonds. The analysis of the DOS is thus consistent with the removal by the field of a few, possibly less stable, Ge-Ge, Se-Se, As-As, and Ge-As bonds responsible for the localized states in the gap.

We remark that the differences in the models Q1–Q4 with and without the electric field must be ascribed to differences already present in the supercooled liquid at 500 K because the models are generated by an abrupt quenching from 500 K to 300 K. To investigate further the structural relaxations that might intervene at lower temperatures, we have also generated two different models by quenching from 500 K to 300 K in four steps for an overall simulation time of 60 ps with or without the electric field. The model generated with the electric field is further equilibrated at 500 K for other 12 ps before the quenching. The electronic DOS of a single snapshot at 300 K of the two models is shown in Fig. 7c, d. The DOS are computed without the electric field. The states at the band edges are less localized that in the models generated by an abrupt quench to 300 K because the system had more time to relax. Still, the electric field leads to an overall widening of the band gap in this latter model as well. We can conclude that an electric field favors the removal of less stable local configurations (less polar bonds) responsible for localized states in the gap. Once more, this feature supports the second assumption of the GBG model on the behavior at the cathode.

A recent theoretical paper[55] shows that V_T decreases by widening the energy window of the band tail (Urbach tail) states. The DFT calculations suggest that the energy window of valence band tail states increases at the anode by electron charging, and on contrary, the energy window of conduction band tail states shrinks at the cathode due to the electric field. This effect can be seen as a local change of the effective gap, which is embodied in the GBG model.

We now briefly comment on previous works on the DFT simulations of the effect of the electric field on the in-gap states in chalcogenide alloys. In ref. 29 and references therein from the same group, it was shown that the application of an electric field of 0.87 V/nm at clamped ions within the Berry's phase approach leads to a very large Stark effect in GeSe with an almost closed band gap. This behavior would be consistent with the field-induced delocalization of tail states discussed, for instance, in ref. 56. In this respect, we remark that in the present article, we have always considered the change in the energy of localized states due to the structural relaxations induced by the electric field and not the energy shift (Stark effect) due to the field itself at clamped ions. All the electronic DOS that we have shown in the present article have been computed without the electric field. However, we checked that in our models, the energy shift of in-gap KS states at clamped ions due to an electric field of 0.5 V/nm (also applied in three orthogonal directions) is at most 0.043 eV. This was also checked by using both the CP2k[57] and the Quantum-ESPRESSO code[58]. We also mention that a band gap closure similar to that found for GeSe by Clima et al.[28] has been found in a more recent study of $GeSe_2$[59], in which an electric field of increasing strength up to 1.5 V/nm was applied during an MD simulation. This behavior cannot be ascribed to a simple Stark effect that could fit the energy shift at low field but not at high field, where structural changes induced by the field are also important. This effect is, however, reversible as the in-gap states closing the gap annihilate once the field is removed[59]. Moreover, a significant redshift of the localized states is observed for fields of and larger than 1 V/nm, which is about five times larger than the typical threshold field in selectors. We must also remark once more that the nature of localized defect states is different in Se-rich $GeSe_2$ and GeSe. In this respect, we also mention that the application of an electric field of 0.25 V/nm in DFT models of $Ge_2Sb_2Te_5$, induces structural relaxations that lead to the removal of in-gap states[60].

Conclusions

In summary, we have developed a microscopic model for the operation of the single chalcogenide X-point memory suitable to explain the dependence of the threshold voltage V_T on the polarity of the applied electric field. The model is consistent with our most recent understanding of the mechanism of OTS, which is based on a bipolar impact ionization avalanche with a different mobility of electrons and holes via a trap-to-trap conduction process, through states outside the mobility gap[32]. The present model for SXM operation was inferred from both experimental measurements and DFT electronic structure calculations. Electrical characterization of a cell made of two chalcogenide slabs with different compositions allowed us to exclude that the polarity-dependent V_T was due to a de-mixing of the alloys as previously proposed in literature. We then proposed a Graded Band Gap (GBG) model in which an inhomogeneous distribution of trap states (localized electronic states in the gap) arises from the combined effect of an electric field at the cathode and a high density of electrons in the conduction band at the anode. DFT calculations show that injected electrons could lead to a redshift of the in-gap states, which come closer to the valence band, while a strong electric field can remove or blueshift in-gap states. This implies a subthreshold current higher when holes are injected at the anode and lower when holes are injected at the cathode, which supports the GBG model. Both these transformations are irreversible, i.e., they persist when either the additional electrons or the electric field are removed. It was also shown that TCAD numerical simulations implementing the GBG model are suitable to reproduce several features of the SXM window (difference between SET and RESET V_T), such as the dependence on temperature and on the thickness and ionicity of the chalcogenide. The microscopic understanding of the SXM device provided by the GBG model will be extremely useful for the optimization and scaling of the memory cell and for future exploration of different alloy compositions in the perspective to exploit this architecture for storage-class memories and other advanced devices.

Methods

Experiments

Capacitor structures with bi-layered chalcogenide reported in Fig. 2 have been fabricated by PVD RF sputtering deposition of all the materials in the Carbon/GAS/Carbon stack and then by patterning the capacitor structure through a standard litho-and-etch process, granting an overall reduced thermal budget to prevent process-induced elemental interdiffusion between the two chalcogenide layers. The maximum process temperature

for the fabrication of stacked capacitors was 250 °C, a value below T_g of both single layers to prevent bilayer mixing. The composition of each chalcogenide sublayer was measured through X-Ray fluorescence spectroscopy (XRF), and optical bandgap (BG) was extracted by Tauc plot from ellipsometric measurements on a 24 mn thick film for each single sublayer (Supplementary Fig. 1). Optical BG results are consistently higher for ch-rich alloy than for ch-poor alloy (Supplementary Table 1). The capacitor with size from 50 to 150 µm was fabricated with GAS bilayer consisting of two sublayers 12 nm thick each. Quasi-static *I*–*V* curves have been collected with a Keysight B1500A semiconductor device parameter analyzer by forcing a voltage on the top electrode and measuring the current entering the top electrode. Device testing temperature was controlled through a thermoschuck and measurements have been performed at different temperatures in the range 25–85 °C. The corresponding conduction activation energy was extracted based on the Poole-Frenkel model. Samples with Se-poor/Se-rich stack sequence pretty overlap with data of reversed one, excluding a significant impact of the deposition sequence. The maximum applied voltage has been kept well below the threshold voltage of these devices. TEM lamella has been prepared with FIB (ThermoFisher Helios 5 DualBeam) on few cells of a large Xpoint SXM array device with 20 nm half pitch[22] in virgin and programmed states (both polarities). The lamella, prepared with special care, included the full cell device without any modification of chalcogenide material, which remained fully embedded inside the surrounding dielectrics and electrodes inside the ~50–60 nm thick lamella. Cell EDX TEM analysis has been performed by means of JEOL JEM-ARM200F microscope equipped with ThermoFisher Noran microanalysis EDS detector; element profiles between the electrodes of four virgin and programmed cells are reported in Fig. 2e, f. All the electrical data reported in Fig. 5 have been measured on 20 nm SXM cells. Quasi-static *I*–*V* curves have been measured with the same experimental setup adopted for the capacitor structures in Fig. 2. For the V_T and SXM window measurement, voltage programming and reading pulses have been applied with a Keysight B1500A semiconductor device parameter analyzer (equipped with a HV-SPGU high-voltage pulse generator unit). Applied pulses have been measured on a Tektronix DPO7254 5600 digital oscilloscope. At the same time, the current flowing through the cell is measured on a second channel of the scope, thus allowing detecting the exact timing of the transition from the OFF-state to the ON-state and to quote the corresponding applied voltage (threshold voltage V_T). Since the OFF-state current just below threshold is around some hundreds of nA, the voltage drops caused by the current flowing on the external routing to connect the cell are in the range of few mV, and it can be easily neglected. SXM window is measured by detecting the V_T of a first programmed high-V_T state and then reprogramming and reading the same cell in the low-V_T state.

TCAD simulations

TCAD simulations were carried out with the commercial software Sentaurus Device by Synopsys[61]. It solves the classical Drift-Diffusion equations for semiconductor transport self-consistently with the Poisson equation for the potential. The TAPF mechanism in Fig. 4a was included in the simulation by instantiating traps in the chalcogenide region coupled with the contact regions via nonlocal tunneling and activating the standard PF model for carrier emission from traps. The activation energy for the subthreshold current depends on the difference between the Fermi level and the valence mobility edge. Implementation of the Graded Band Gap model (Fig. 4a) and, especially, of the band edge gradient effect on the impact ionization coefficient (Eq. 1) was not trivial, and has required some development to extend the capability of the simulation tool. *I*–*V* simulations were done in stationary conditions by assuming $E_{A\_Anode} = 0.51$ eV and $E_{A\_Cathode} = E_{A\_anode} + 0.07$ eV for the asymmetric activation energy at the two electrode. We used current boundary conditions to allow simulating of the snap-back. However, sometimes simulations failed to converge once in the snap-back region because of the difficult numerical problem in this condition (Fig. 5a). Nevertheless, the threshold point was always visible, allowing to correctly compute the SXM memory window.

DFT simulations

We performed DFT-MD simulations using the CP2k suite of programs[57] with norm-conserving pseudopotentials with four, five, and six valence electrons for Ge, As, and Se[62]. The Kohn-Sham orbitals were expanded in the basis set of triple-zeta-valence plus polarization Gaussian-type orbitals (GTO), while the charge density was expanded in a planewave basis set with a cutoff of 240 Ry to efficiently solve the Poisson equation within the Quickstep scheme[7,57]. MD simulations in supercells with periodic boundary conditions were performed by using the predictor-corrector scheme of refs. 63,64. for the self-consistent solution of KS equation at each MD step. In the spirit of the Car-Parrinello (CP) approach[65], the wave functions are not self-consistently optimized during the dynamics. However, in contrast to CP, large integration time steps can be used in the simulation. This scheme leads to a slightly dissipative dynamics of the type $-\gamma \dot{\boldsymbol{R}} I$ where $\boldsymbol{R}_I$ are the ionic coordinates. In refs. 63,64. It is shown how to compensate for this dissipation and obtain a correct canonical sampling by applying a Langevin thermostat. The same scheme was applied in our previous works on the amorphous phase of telluride alloys[66–68]. MD simulations have been performed at constant volume (fixed simulation cell) and constant temperature enforced by a Langevin thermostat as mentioned above. Brillouin Zone integration was restricted to the supercell Γ-point, and a time step of 1.5 fs was used. We employed the generalized gradient approximation to the exchange-correlation functional due to Becke-Lee-Yang-Parr (BLYP)[69,70] that was shown to reproduce well the structural properties of liquid and amorphous $GeSe_2$ and GeSe compounds[71,72].

The amorphous GAS234 models contain 300 atoms in cubic box with an edge of 20.413 Å, corresponding to a density of 0.0352 atoms/Å^3 which was assigned in turn by interpolation of the experimental densities from neighbor compositions given in ref. 73,74. The amorphous models (M1-M4) were generated by quenching from 1200 K to 300 K in about 120 ps. The atomic positions of the a-GAS234 models equilibrated at 300 K were then optimized at zero temperature. The model M1 and M4 are actually not fully independent. In fact, they were generated in the last step of quenching from 500 K to 300 K from two snapshots of the same trajectory at 500 K separated by a short time interval. We followed this procedure to check the dependence of the structural and electronic properties of the models on the very last step of the quenching. Models M1 and M4 are structurally rather similar, and both feature the same structural unit consisting of a As-Se-As-As-As-Ge chain on which the LUMO state is localized. However, the second coordination shell of the atoms belonging to this chain differs in the two models, which leads to a different response of the LUMO state to electron charging and to the electric field, as we discussed in the article.

To quantify the localization properties of individual KS states, we computed the inverse participation ratio (IPR), which is defined for the i-th KS state by $\sum_j c_{ij}^4 / \left(\sum_j c_{ij}^2\right)^2$, where j runs over the GTOs of the basis set, and c_{ij} are the expansion coefficients of the i-th KS state in GTOs. The IPR takes values varying from 1/N for a completely delocalized electron, where N is the number of atomic-like orbitals in the basis set of the whole supercell, to one for an electron completely localized on a single atomic-like orbital.

A uniform electric field is introduced in the total energy as a term $-\boldsymbol{P}\cdot\boldsymbol{F}$ where $\boldsymbol{P}$ is the dipole moment computed within Berry's phase approach[52,53]. The dipole moment is defined only modulo the quantum of polarization, which amounts to transfer an electron by the primitive Bravais vectors of the supercell. This scheme allows introducing a uniform electric field by still keeping the periodic boundary conditions. This scheme can be applied in the presence of an electronic gap between delocalized states sufficiently large to prevent the Zener breakdown.

Data availability

The data that support the findings of this study are available from the corresponding author upon reasonable request and compliant with Micron IPs.

Received: 29 March 2025; Accepted: 11 December 2025;
Published online: 10 January 2026

References

1. Ovshinsky, S. R. Reversible electrical switching phenomena in disordered structures. *Phys. Rev. Lett*. **21**, 1450–1453 (1968).
2. Pirovano, A., Lacaita, A., Benvenuti, A., Pellizzer, F. & Bez, R. Electronic switching in phase-change memories. In *Proc. IEEE Transactions on Electron Devices*. Vol. 51, 452–459 (IEEE, 2004).
3. Wuttig, M. & Yamada, N. Phase-change materials for rewriteable data storage. *Nat. Mater*. **6**, 824–832 (2007).
4. Noé, P., Vallée, C., Hippert, F., Fillot, F. & Raty, J.-Y. Phase-change materials for non-volatile memory devices: from technological challenges to materials science issues. *Semicond. Sci. Technol.* **33**, 013002 (2018).
5. Zhang, W., Mazzarello, R., Wuttig, M. & Ma, E. Designing crystallization in phase-change materials for universal memory and neuro-inspired computing. *Nat. Rev. Mater.* **4**, 150–168 (2019).
6. Fantini, P. Phase change memory applications: the history, the present and the future. *J. Phys. D Appl. Phys.* **53**, 283002 (2020).
7. Fong, S. W., Neumann, C. M. & Wong, H.-S. P. Phase-change memory—towards a storage-class memory. *IEEE Trans. Electron Dev.* **64**, 4374–4385 (2017).
8. Cappelletti, P. et al. Phase change memory for automotive grade embedded NVM applications. *J. Phys. D Appl. Phys.* **53**, 193002 (2020).
9. Redaelli, A., Petroni, E. & Annunziata, R. Material and process engineering challenges in Ge-rich GST for embedded PCM. *Mater. Sci. Semicond. Process.* **137**, 106184 (2022).
10. Kuzum, D., Jeyasingh, R. G., Lee, B. & Wong, H.-S. P. Nanoelectronic programmable synapses based on phase change materials for brain-inspired computing. *Nano Lett.* **12**, 2179–2186 (2012).
11. Tuma, T., Pantazi, A., Le Gallo, M., Sebastian, A. & Eleftheriou, E. Stochastic phase-change neurons. *Nat. Nanotechnol.* **11**, 693–699 (2016).
12. Sebastian, A., Le Gallo, M., Khaddam-Aljameh, R. & Eleftheriou, E. Memory devices and applications for in-memory computing. *Nat. Nanotechnol.* **15**, 529–544 (2020).
13. Cheng, H.-Y., Carta, F., Chien, W. C., Lung, H.-L. & BrightSky, M. J. 3D cross-point phase-change memory for storage-class memory. *J. Phys. D Appl. Phys.* **52**, 473002 (2019).
14. Zhao, Z. et al. Chalcogenide Ovonic Threshold Switching Selector. *Nano Micro Lett.* **16**, 81 (2024).
15. Kau, D. et al. A stackable cross-point Phase Change Memory. In *Proc. IEEE International Electron Devices Meeting (IEDM)* 1–4 (IEEE, 2009).
16. Fazio, A. In-memory computing for machine learning and deep learning. In *Proc. IEEE International Electron Devices Meeting (IEDM)* 24.1.1–24.1.4. (IEEE, 2020).
17. Alayan, M. et al. In-depth investigation of programming and reading operations in RRAM cells integrated with Ovonic Threshold Switching (OTS) selectors. In *2017 IEEE International Electron Devices Meeting (IEDM)* 2.3.1-2.3.4 (San Francisco, CA, USA, 2017).
18. Tortorelli, I., Tang, S. & Papagianni, C. Apparatuses and methods including memory and operation of same, US patent 10134470, Sept. (2018).
19. Ravsher, T. et al. Polarity-dependent threshold voltage shift in ovonic threshold switches: Challenges and opportunities. In *Proc. IEEE International Electron Devices Meeting (IEDM)* 28.4.1–28.4.4. (IEEE, 2021).
20. Ravsher, T. et al. Polarity-induced threshold voltage shift in ovonic threshold switching chalcogenides and the impact of material composition. *Phys. Status Solidi RRL* **17**, 2200417 (2023).
21. S. Hong et al. "Extremely high performance, high density 20nm self-selecting cross-point memory for Compute Express Link," *2022 International Electron Devices Meeting (IEDM)*, 18.6.1-18.6.4 (San Francisco, CA, USA, 2022).
22. Pellizzer F. et al. Polarity-dependent threshold voltage shift in ovonic threshold switches: Challenges and opportunities. In *Proc. IEEE International Electron Devices Meeting (IEDM)* 1–4 https://doi.org/10.1109/IEDM45741.2023.10413669 (IEEE, 2023).
23. Park, I.-M. et al. Enhanced Endurance Characteristics in High Performance 16nm Selector Only Memory (SOM). In *2023 International Electron Devices Meeting (IEDM)*, 1–4 (San Francisco, CA, USA, 2023).
24. Ravsher, T. et al. Evidence of heat-assisted atomic migration in GeSe self-selecting memory at high operating current density. *Phys. Status Solidi RRL* **18**, 2300415 (2024).
25. Liu, Z.-L. et al. A $Ge_{(x)}Se_{(1-x)}$ switch-only-memory technology through polarized atomic distribution. *Sci. Rep.* **14**, 22115 (2024).
26. Ravsher, T. et al. Comprehensive Performance and Reliability Assessment of Se-based Selector-Only Memory. In *2024 IEEE International Reliability Physics Symposium (IRPS)*, pp. 7A.5-1-7A.5-9, (Grapevine, TX, USA, 2024).
27. Clima, S. et al. Selector Only Memory: Exploring Atomic Mechanisms from First-Principles. In *Proc. IEEE International Electron Devices Meeting (IEDM)* 1–4 (IEEE, 2024).
28. Clima, S. et al. Ovonic Threshold-Switching Ge_xSe_y Chalcogenide Materials: Stoichiometry, Trap Nature, and Material Relaxation from First Principles. *Phys. Status Solidi RRL* **14**, 1900672 (2020).
29. Clima, S. et al. Ovonic threshold switch chalcogenides: connecting the first-principles electronic structure to selector device parameters. *ACS Appl. Electron. Mater.* **5**, 461–469 (2023).
30. Lee, J. et al. Understanding switching mechanism of selector-only memory using Se-based Ovonic threshold switch device. *IEEE Trans. Electron Dev.* **71**, 3351–3357 (2024).
31. Sung, H. J. et al. Microscopic Origin of Polarity-Dependent V_{TH} shift in amorphous chalcogenides for 3d self-selecting memory. *Adv. Sci.* **11**, 2408028 (2024).
32. Fantini, P., Polino, N., Ghetti, A. & Ielmini, D. Threshold switching by bipolar avalanche multiplication in ovonic chalcogenide glasses. *Adv. Electr. Mat.* **9**, 2300037 (2023).
33. Fantini, P. et al. Threshold switching in a-Si and a-Ge-based MSM selectors and its implications for device reliability. In *Proc. IEEE International Electron Devices Meeting (IEDM)* 1–4 (IEEE, 2021).
34. Fantini, P., Ferro, M. & Calderoni, A. Field-accelerated structural relaxation in the amorphous state of phase change memory. *Appl. Phys. Lett.* **102**, 253505 (2013).
35. Jeong, D. S. & Hwang, C. S. Tunneling-assisted Poole-Frenkel conduction mechanism in HfO_2 thin films. *J. App. Phys.* **98**, 113701 (2005).
36. Arutyunyan, V. M. & Petrosyan, S. G. Avalanche multiplication in graded band gap structures. *Infrared Phys* **29**, 681–684 (1988).
37. Lencer, D. et al. A map for phase-change materials. *Nat. Mater* **7**, 972–977 (2008).
38. Cheng, H. Y. et al. An ultra-high endurance and thermally stable selector based on TeAsGeSiSe chalcogenides compatible with BEOL IC Integration for cross-point PCM. In *Proc. IEEE International Electron Devices Meeting (IEDM)* 37.3.1–37.3.4 (IEEE, 2018).
39. Cheng, H. Y. et al. Optimizing AsSeGe chalcogenides by dopants for extremely low IOFF, high endurance and low Vth drift 3D crosspoint memory. In *Proc. IEEE International Electron Devices Meeting (IEDM)* 28.6.1–28.6.4 (IEEE, 2021).
40. Caravati, S., Baratella, D., Fantini, P. & Bernasconi, M. In-gap electronic states of GeAsSe and SiGeAsSe alloys for selector devices from atomistic simulations. *Solid State Sci.* **170**, 108127 (2025).
41. Marzari, N. & Vanderbilt, D. Maximally localized generalized Wannier functions for composite energy bands. *Phys. Rev. B* **56**, 12847–12865 (1997).

42. Vaughn, D. D., Patel, R. J., Hickner, M. A. & Schaak, R. E. Single-crystal colloidal nanosheets of GeS and GeSe. *J. Am. Chem. Soc.* **132**, 15170–15172 (2010).
43. Dittmar, G. & Schaefer, H. Die Kristallstruktur von Germaniumdiselenid. *Acta Crystallogr. B* **32**, 2726–2728 (1976).
44. Shimakawa, K. On the compositional dependence of the optical gap in amorphous semiconducting alloys. *J. Non Cryst. Solids* **43**, 229 (1981).
45. Xu, M., Xu, Mi. & Miao, X. Deep machine learning unravels the structural origin of mid-gap states in chalcogenide glass for high-density memory integration. *InfoMat* **4**, e12315 (2022).
46. Jacoboni, C. Piccini, E. Brunetti, R. & Rudan, M. Time- and space-dependent electric response of Ovonic devices. *J. Phys. D* **50**, 255103 (2017).
47. Slassi, A. et al. Device-to-materials pathway for electron traps detection in amorphous GeSe-based selectors. *Adv. Electron. Mater.* **9**, 2201224 (2023).
48. Raty, J.-Y. & Noé, P. Ovonic threshold switching in Se-rich Ge_xSe_{1-x} glasses from an atomistic point of view: the crucial role of the metavalent bonding mechanism. *Phys. Status Solidi RRL* **14**, 2070024 (2020).
49. Noé, P. et al. Toward ultimate nonvolatile resistive memories: the mechanism behind ovonic threshold switching revealed. *Sci. Adv.* **6**, eaay2830 (2020).
50. Guo, Y., Li, H., Zhang, W. & Robertson, J. Structural changes during the switching transition of chalcogenide selector devices. *Appl. Phys. Lett.* **115**, 163503 (2019).
51. Konstantinou, K., Mocanu, F. C., Lee, T.-H. & Elliott, S. R. Revealing the intrinsic nature of the mid-gap defects in amorphous $Ge_2Sb_2Te_5$. *Nat. Comm*. **10**, 3065 (2019).
52. Souza, I., Iñiguez, J. & Vanderbilt, D. First-principles approach to insulators in finite electric fields. *Phys. Rev. Lett.* **89**, 117602 (2002).
53. Umari, P. & Pasquarello, A. Ab initio molecular dynamics in a finite homogeneous electric field. *Phys. Rev. Lett.* **89**, 157602 (2002).
54. Grundmann, M. *The Physics of Semiconductors* (Springer International Publishing Switzerland, 2016).
55. Brunetti, R., Jacoboni, C. & Rudan, M. The role of band-tail states on the electric properties of amorphous chalcogenides: a simulative approach. *J. Appl. Phys.* **136**, 085701 (2024).
56. Nardone, M., Simon, M., Karpov, I. V. & Karpov, V. G. Electrical conduction in chalcogenide glasses of phase change memory. *J. Appl. Phys.* **112**, 071101 (2012).
57. VandeVondele, J. et al. Quickstep: fast and accurate density functional calculations using a mixed Gaussian and plane waves approach. *Comput. Phys. Commun.* **167**, 103–128 (2005).
58. Giannozzi, P. et al. QUANTUM ESPRESSO: a modular and open-source software project for quantum simulations of materials. *J. Phys. Condens. Matter* **21**, 395502 (2009).
59. Zhang, X., Li, K., Zhou, J., Elliott, S. R. & Sun, Z. Ovonic threshold switching induced by reversal of Peierls-like distortion in $GeSe_2$ glass. *Adv. Electron. Mater*. **37**, 2400291 (2024).
60. Konstantinou, K., Mocanu, F. C., Akola, J. & Elliott, S. R. Electric-field-induced annihilation of localized gap defect states in amorphous phase-change memory materials. *Acta Mater.* **223**, 117465 (2022).
61. Sentaurus TCAD tools, Synopsys, Mountain View, https://www.synopsys.com/manufacturing/tcad/device-simulation/sentaurus-device.html 2022.
62. Goedecker, S., Teter, M. & Hutter, J. Separable dual-space Gaussian pseudopotentials. *Phys. Rev. B* **54**, 1703–1710 (1996).
63. Kühne, T. D., Krack, M., Mohamed, F. R. & Parrinello, M. Efficient and accurate Car-Parrinello-like approach to Born-Oppenheimer molecular dynamics. *Phys. Rev. Lett.* **98**, 066401 (2007).
64. Kühne, T. D., Krack, M. & Parrinello, M. Static and dynamical properties of liquid water from first principles by a novel Car-Parrinello-like approach. *J. Chem. Theory Comput.* **5**, 235–241 (2009).
65. Car, R. & Parrinello, M. Unified approach for molecular dynamics and density-functional theory. *Phys. Rev. Lett.* **55**, 2471–2474 (1985).
66. Caravati, S., Bernasconi, M., Kuehne, T. D., Krack, M. & Parrinello, M. Coexistence of tetrahedral- and octahedral-like sites in amorphous phase change materials. *Appl. Phys. Lett.* **91**, 171906 (2007).
67. Caravati, S., Bernasconi, M. & Parrinello, M. First-principles study of liquid and amorphousSb_2Te_3. *Phys. Rev. B* **81**, 014201 (2010).
68. Spreafico, E., Caravati, S. & Bernasconi, M. First-principles study of liquid and amorphous $InGeTe_2$. *Phys. Rev. B* **83**, 144205 (2011).
69. Becke, A. D. Density-functional exchange-energy approximation with correct asymptotic behavior. *Phys. Rev. A* **38**, 3098–3100 (1988).
70. Lee, C., Yang, W. & Parr, R. G. Development of the Colle-Salvetti correlation-energy formula into a functional of the electron density. *Phys. Rev. B* **37**, 785–789 (1988).
71. Micoulaut, M., Vuilleumier, R. & Massobrio, C. Improved modeling of liquid $GeSe_2$: impact of the exchange-correlation functional. *Phys. Rev. B* **79**, 214205 (2009).
72. Le Roux, S., Bouzid, A., Boero, M. & Massobrio, C. The structure of liquid GeSe revisited: a first principles molecular dynamics study. *J. Chem. Phys.* **138**, 174505 (2013).
73. Wang, R. P., Smith, A., Luther-Davies, B., Kokkonen, H. & Jackson, I. Observation of two elastic thresholds in GexAsySe1-x-y glasses. *J. Appl. Phys.* **105**, 056109 (2009).
74. Wang, T. et al. Elastic transition thresholds in Ge–As(Sb)–Se glasses. *J. Phys. D Appl. Phys.* **46**, 165302 (2013).

Acknowledgements

Micron Authors acknowledge all Micron colleagues who worked to make SXM chips a reality.

Author contributions

P. Fantini, A. Ghetti, E. Varesi, A. Pirovano, F. Pellizzer, and R. Bez collected and analyzed the experimental data, developed the TCAD model, and ran simulations. D. Baratella, C. Ribaldone, S. Caravati, D. Campi, and M. Bernasconi performed the DFT simulations. The entire list of authors contributed to the interpretation of the experimental and theoretical results in a series of discussions that led to this work.

Competing interests

The authors declare no competing interests.

Additional information

Supplementary information The online version contains supplementary material available at https://doi.org/10.1038/s43246-025-01044-2.

Correspondence and requests for materials should be addressed to Paolo Fantini.

Peer review information *Communications Materials* thanks Min Zhu and the other, anonymous, reviewer(s) for their contribution to the peer review of this work. A peer review file is available.